

# Origin and Evolution of Ultraflatbands in Twisted Bilayer Transition Metal Dichalcogenides: Realization of Triangular Quantum Dot Array

Mit H. Naik,<sup>1,\*</sup> Sudipta Kundu,<sup>1</sup> Indrajit Maity,<sup>1</sup> and Manish Jain<sup>1,†</sup>

<sup>1</sup>*Center for Condensed Matter Theory, Department of Physics,  
Indian Institute of Science, Bangalore 560012, India*

(Dated: April 8, 2024)

## Abstract

Using a multiscale computational approach, we probe the origin and evolution of ultraflatbands in moiré superlattices of twisted bilayer MoS<sub>2</sub>, a prototypical transition metal dichalcogenide. Unlike twisted bilayer graphene, we find no unique magic angles in twisted bilayer MoS<sub>2</sub> for flatband formation. Ultraflatbands form at the valence band edge for twist angles ( $\theta$ ) close to 0° and at *both* the valence and conduction band edges for  $\theta$  close to 60°, and have distinct origins. For  $\theta$  close to 0°, inhomogeneous hybridization in the reconstructed moiré superlattice is sufficient to explain the formation of flatbands. For  $\theta$  close to 60°, additionally, local strains cause the formation of modulating triangular potential wells such that electrons and holes are spatially separated. This leads to multiple energy-separated ultraflatbands at the band edges closely resembling eigenfunctions of a quantum particle in an equilateral triangle well. Twisted bilayer transition metal dichalcogenides are thus suitable candidates for the realisation of ordered quantum dot array.

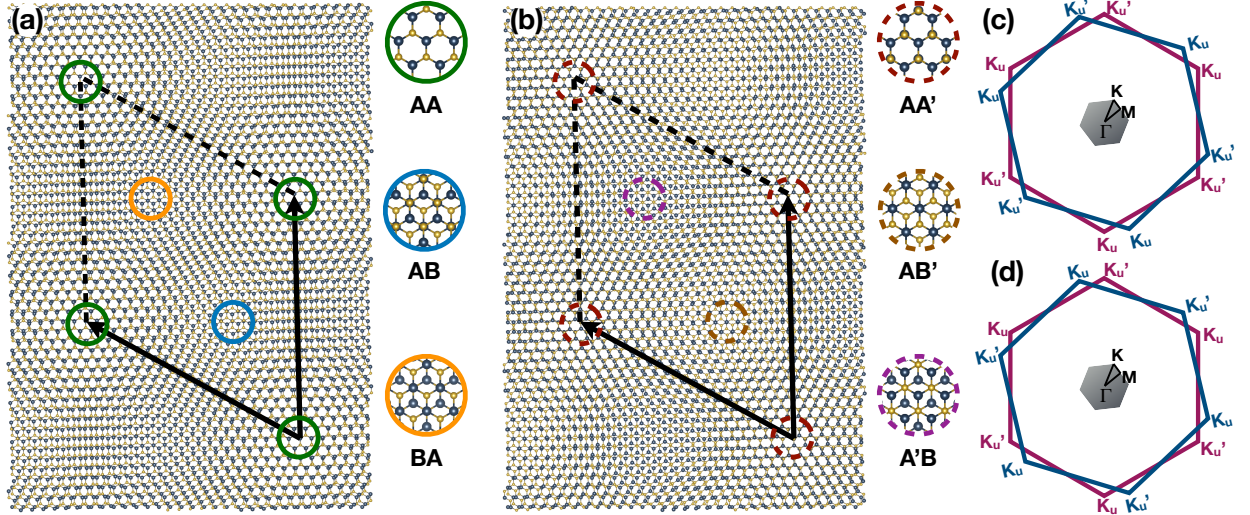


FIG. 1. (a) and (b) Structure of  $2.65^\circ$  and  $57.35^\circ$  rigidly twisted bilayer MoS<sub>2</sub>. The moiré pattern is composed of various stackings. The high-symmetry stackings are identified using circles. The moiré superlattice vectors are shown with black arrows. (c) and (d) Schematic of the unit-cell Brillouin zone (BZ) of the bottom (in magenta) and top (blue) layer for a twist angle close to  $0^\circ$  and  $60^\circ$ , respectively. The moiré BZ is shown in gray and the path connecting the  $\Gamma$ , M and K points, along which the band structure is plotted, is marked.

## I. INTRODUCTION

Correlated insulating behaviour and unconventional superconductivity was recently observed in twisted bilayer graphene (TBG) at a 'magic' angle of  $1.1^\circ$ <sup>1–3</sup>. While the nature of superconductivity is still contested, formation of ultraflatbands near the Fermi level at this angle is essential to understanding these phenomena<sup>4–11</sup>. Since this discovery, ultraflatbands have been predicted in other twisted 2D materials<sup>12–18</sup> including small angle twisted bilayer MoS<sub>2</sub> (TBM), a prototypical transition metal dichalcogenide (TMD)<sup>19,20</sup>. For TBG, the bands flatten in a narrow range of  $0.1^\circ$  about  $1.1^\circ$ <sup>21,22</sup>, making their experimental realisation challenging. The existence or absence of similar unique 'magic' angles in twisted TMDs has not been explored. Ultraflatbands and localization also has significant implications on optical properties of the material<sup>23,24</sup>.

The structural properties of twisted TMDs are remarkably different from TBG. Due to sublattice symmetry breaking in the TMDs, distinct moiré patterns form for twist angles

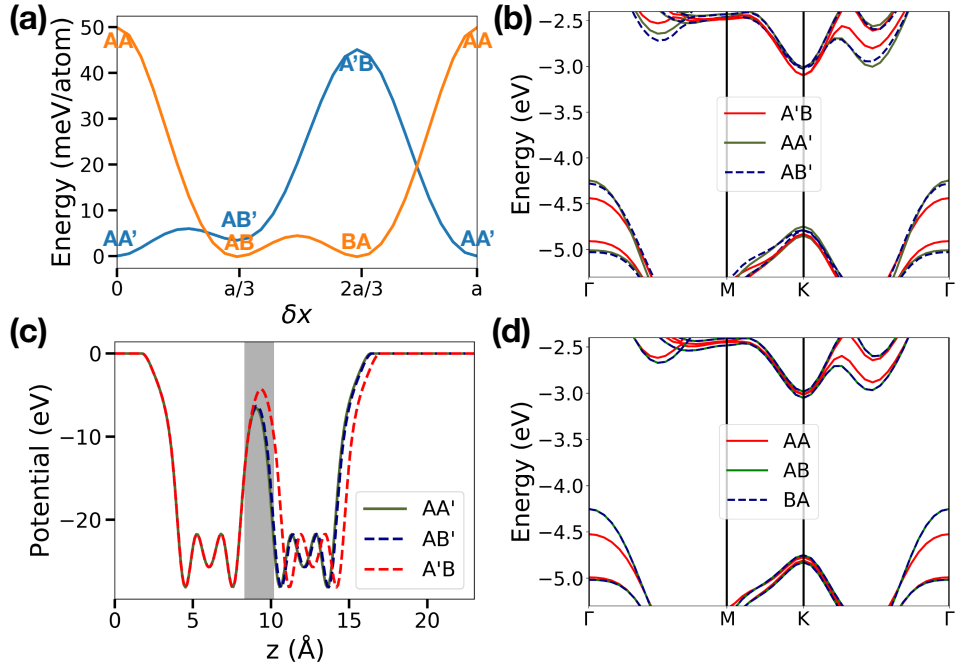


FIG. 2. (a) Relative energy of the stackings as a function of sliding the top layer with respect to the bottom layer along the arm-chair direction in the unit-cell. The starting configuration ( $\delta x = 0$ ) is AA' and AA stacking for the blue and orange curve, respectively. (b) and (d) Electronic band structure of the isolated (unit-cell) high-symmetry stackings in Fig. 1. (c) Planar-averaged DFT potential of the isolated high-symmetry stackings. The shaded area marks the potential barrier between the layers. In (b), (c) and (d) the spacing between the layers for each stacking is taken from the corresponding region in the relaxed 2° and 58° twisted bilayer MoS<sub>2</sub> moiré superlattices.

close to 0° and 60°<sup>19</sup>. As the twist-angle approaches 0° or 60°, the moiré length scale increases. The sliding potential energy landscape in twisted TMDs is more corrugated compared to TBG leading to larger deformation of the moiré superlattice<sup>25–27</sup>. These deformations involve a change in the distribution of stackings and interlayer spacings from the rigidly twisted structure<sup>19,27,28</sup>. The relaxed moiré pattern for twist angles ( $\theta$ ) close to 0° is similar to twisted bilayer graphene. The low-energy bernal stacking occupies large equilateral triangle areas separated by shear-strain solitons, while the higher energy AA stacking region is reduced in size. The relaxed moiré pattern for twist angle close to 60°, on the other hand, is strikingly different<sup>27,29,30</sup>. For  $\theta > 56^\circ$ , the AA' stacking region occupies the largest area, transforming from an equilateral triangle to a Reuleaux triangle<sup>27,28</sup>. This leads to a

reduction of the rotational symmetry of the moiré superlattice from six-fold to three-fold.

The electronic structure of twisted TMDs is strongly influenced by the structural transformation of the moiré superlattice. Neglecting structural relaxations in the simulation of these systems leads to spurious localisation of flatbands<sup>19</sup>. For  $\theta = 3.5^\circ$ , the flatband states close to the valence band maximum localise to the bernal stacking sites, forming an extended hexagonal network in the moiré. For  $\theta = 56.5^\circ$ , on the other hand, the valence band edge states have a smaller bandwidth and localise at the AA' stacking. However, the presence or absence of unique 'magic' angles for flatband formation and the influence of the reuleaux triangle pattern (for  $\theta > 56.5^\circ$ ) on the electronic structure have not been explored and are important to complete our understanding of twisted bilayer TMDs. First-principles study of the electronic structure of the relaxed moiré pattern for  $\theta > 56.5^\circ$  and  $\theta < 3.5^\circ$  is computationally challenging due to the large number of atoms ( $> 1600$ ) involved in the simulation.

Quantum dots resemble artificial atoms with sizes in the order of nanometers.<sup>31,32</sup> Quantum dots using 2D materials have several potential applications including quantum emission, design of solar cells and photocatalysis<sup>33–38</sup>. The current route to obtain quantum dots is through preparation of a colloidal suspension of 2D material flakes<sup>34–36,39</sup>. This leads to poor control over the size and shape of quantum dots<sup>37</sup>. Obtaining quantum dot array in a dry and systematic manner has been a challenge<sup>39</sup>. While the possibility of obtaining quantum dots in moiré patterns of twisted bilayers has been proposed<sup>33,40,41</sup>, explicit predictive calculations on the moiré pattern including crucial atomic relaxation effects are lacking. The scope of TBG for quantum dot applications is strongly limited by the band gap and formation of these flatbands only at  $1.1^\circ$  twist-angle<sup>21,22</sup>. Moiré patterns constructed using transition metal dichalcogenides (TMDs), on the other hand, hold more promise with recent photoluminescence measurements showing signatures of localised excitons in the moiré superlattice<sup>24,42–46</sup>.

In this article, we use an efficient multiscale approach to study the origin and evolution of ultraflatbands in TBM. We establish, that unlike TBG, there are no unique magic angles in TBM for the formation of ultraflatbands. Ultraflatbands form at the valence band edge for twist angles ( $\theta$ ) close to  $0^\circ$  and  $60^\circ$ . The electronic structure for  $\theta$  close to  $60^\circ$  is strikingly different from  $0^\circ$ . Multiple energy-separated ultraflatbands form at both the valence and conduction band edges for  $\theta > 56^\circ$ . Our calculations reveal a modulating potential well in

the moiré superlattice which leads to spatially separated electrons and holes. The ordering, real-space distribution and the degeneracies of the ultraflatbands at the valence band edge are in excellent agreement with states of a quantum particle in an infinite equilateral triangle potential well. The wavefunctions at the conduction band edge also resemble triangular well states, with the degeneracies modified by valley degeneracies. The ultraflatbands form due to two factors: 1) inhomogeneity in the interlayer hybridization in the moiré superlattice due to variation in the interlayer spacing, and 2) local strains due to soliton formation. Furthermore, the local strains in each layer modify the electronic structure of the optically active  $K$  valleys of the unit-cell BZ. This could result in confinement of excitons in the moiré pattern.

Twisted bilayer transition metal dichalcogenides are composed of distinct high-symmetry stackings for twist angles close to  $0^\circ$  and  $60^\circ$ . For twist angles close to  $0^\circ$ , the high-symmetry stackings are AA, AB (also referred to as  $B^{Mo/S}$ <sup>19</sup>) and BA ( $B^{S/Mo}$ ). For twist angles close to  $60^\circ$ , the moiré contains AA' (also referred to as AB), A'B ( $B^{S/S}$ ) and AB' ( $B^{Mo/Mo}$ ) high-symmetry stackings (Fig. 1 (a) and (b)). The formation of a moiré superlattice leads to shrinking of the unit-cell Brillouin zone (UBZ), as shown in Fig. 1 (c) and (d). The relative energy of the various stackings in the moiré determines the relaxation pattern<sup>19,26–28</sup>. The AA and A'B stackings are highest in energy (Fig. 2 (a)) due to steric effects associated with S atoms of the bottom layer facing S atoms in the top layer. The AB and BA stackings are equal in energy, while the AA' stacking is lower in energy compared to AB'. This difference leads to different structural relaxations for twist angles close to  $60^\circ$  compared to those close to  $0^\circ$ . The interlayer spacing of the various stackings is also determined by the relative positions of the S atoms in the two layers. The AA and A'B stacking have a larger interlayer spacing, leading to a reduction in hybridisation between the layers. The valence band splittings at the  $\Gamma$  point in the UBZ is controlled by the hybridisation between the layers<sup>47</sup>. The different interlayer spacings for the different stackings leads to the variation in the unit-cell band structure shown in Fig. 2 (b) and (d). The  $\Gamma$  point valence band maximum (VBM) has the character of  $S-p_z$  which make it more sensitive to interlayer spacing than the  $K$  point VBM or conduction band minimum (CBM) (Mo- $d$  character)<sup>47</sup>. The potential barrier between the two layers, as shown in Fig. 2 (c), can be used a measure of the interlayer hybridisation<sup>47</sup>. Larger interlayer spacing between the layers leads to an increase in the height of the barrier.

## II. COMPUTATIONAL DETAILS

The commensurate superlattices for twisted bilayer MoS<sub>2</sub> (TBM) are constructed using the Twister code<sup>19,48</sup>. The twist-angle, number of atoms in the moiré superlattice and length of the superlattice vector in our simulations are provided in Table I. The structural relaxations of TBM are performed with the LAMMPS<sup>49,50</sup> package using intralayer Stillinger-Weber (SW)<sup>51,52</sup> and interlayer Kolmogorov-Crespi (KC) potential. The force minimizations are performed using the conjugate gradient method with a tolerance of  $10^{-6}$  eV/Å. The KC potential has been fit<sup>26</sup> to van der Waals (vdW) corrected DFT calculations. The SW+KC forcefield relaxed structure for TBM has been shown<sup>26</sup> to yield electronic structure in good agreement with the vdW corrected DFT relaxed structure. The unit-cell lattice constant of MoS<sub>2</sub> used in our calculations is 3.14 Å.

The electronic structure calculations are performed on the relaxed moiré superlattice using density functional theory<sup>53</sup> (DFT) calculations with the SIESTA<sup>54</sup> package. The DFT wavefunctions are expanded in a double- $\zeta$  plus polarization basis. Norm-conserving pseudopotentials<sup>55</sup> and the local density approximation to the exchange-correlation functional are employed. Van der Waals corrections only influence the interlayer spacing between the layers in a bilayer system and do not influence the electronic band structure<sup>47</sup>. Since we are working with the relaxed structure of TBM, we do not use any vdW correction while computing the electronic structure. We only sample the  $\Gamma$  point in the moiré Brillouin zone (MBZ) to obtain the converged charge density for the moiré superlattice calculations. For the unit-cell simulations we use a  $12 \times 12 \times 1$  sampling of the unit-cell BZ (UBZ). A plane-wave energy cut-off of 250 Ry is used to generate the 3D grid for the simulation. Spin-orbit coupling leads to a gap opening of 150 meV at the valence band edge at the  $K$  point in all unit-cell stackings. Due to the large difference in the energy between the  $\Gamma$  point VBM and the  $K$  point VBM in the UBZ, spin-orbit coupling effect does not influence the flatbands close to the valence band edge in TBM<sup>19</sup>. Hence, we do not include spin-orbit coupling in our electronic structure calculations.

Twist angle ( $\theta$ )	Number of atoms	Moiré superlattice size (Å)
1.54°	8322	117.1
2.0°	5514	95.3
2.65°	2814	68.1
2.88°	2382	62.6
57.12°	2382	62.6
57.35°	2814	68.1
58.0°	5514	95.3
58.46°	8322	117.1

TABLE I. Twist angles, number of atoms and sizes of the moiré superlattice vector in our calculations. The commensurate superlattices and constructed using the Twister code<sup>48</sup>.

### III. STRUCTURAL RELAXATIONS

Starting with the rigidly twisted structure, upon relaxation, the atoms in each layer locally shear in opposite directions to attain a lower energy stacking<sup>19,56</sup>. This shear leads to an in-plane strain in each layer of the moiré superlattice. The final relaxed pattern is hence a balance between the cost of in-plane strain and stacking energy gain. To describe the redistribution of stackings upon relaxation we will use order parameters<sup>25</sup> (OP),  $\vec{u}$  and  $\vec{v}$ <sup>19</sup>, to describe the local stackings for twist angles close to 0° and 60°, respectively.  $\vec{u}$  for a local stacking is defined as the displacement vector that transforms the stacking to the highest energy AA stacking.  $\vec{v}$  similarly transforms any local stacking in the moiré to the A'B stacking. By definition, smaller the value of  $|\vec{u}|$  or  $|\vec{v}|$  less favourable the stacking. Fig. 3 shows the evolution of the  $|\vec{u}|$  and  $|\vec{v}|$  as a function of twist-angle. The AB and BA regions remain triangles of equal area as twist angle approaches 0°. For twist angles approaching 60°, on the other hand, the AA' stacking region grows appreciably compared to other stackings. The AA' stacking is lower in energy than AB'. Hence the area of AA' stacking in the moiré is larger and leads to a reduced three-fold symmetry around A'B. The domain wall network has the shape of Reuleaux triangles<sup>27,28</sup> in twist angles close to 60°, as opposed to equilateral triangles in twist angles close to 0°. This contrast in the relaxation pattern leads to different electronic structure for twist angles close to 0° and 60°. Furthermore, atomic displacements

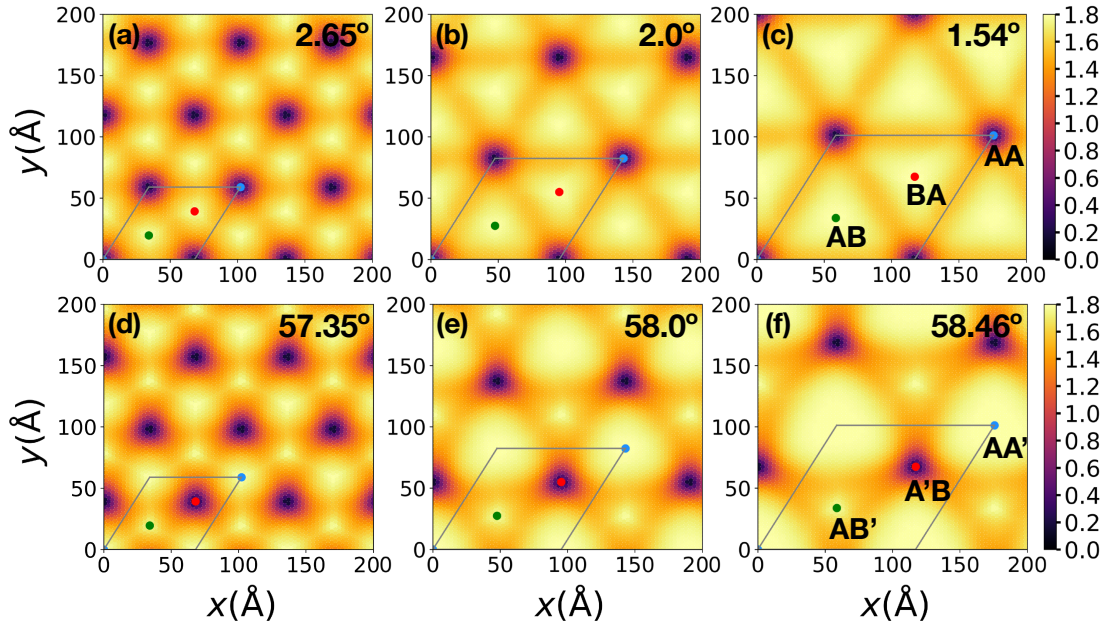


FIG. 3. (a), (b) and (c) ((d), (e) and (f)) Order parameter distribution in  $2.65^\circ$ ,  $2.0^\circ$  and  $1.54^\circ$  ( $57.35^\circ$ ,  $58.0^\circ$  and  $58.46^\circ$ ) twisted bilayer MoS<sub>2</sub>, respectively.

in the out-of-plane direction lead to an undulating interlayer spacing in the moiré<sup>19,27</sup>. The local interlayer spacing in the moiré (Fig. 4) is characteristic of the local stacking. The A'B stacking has the largest interlayer spacing due to Pauli repulsion owing to sulfur atoms in the bottom layer facing sulfur atoms in the top layer. The lattice reconstruction leads to the formation of an inhomogeneous strain distribution in the moiré (Fig. 5). The strain is localised along the soliton regions. Within each soliton region a network of tensile and compressive strain lines is formed. The magnitude and direction of these strains is switched between the top and bottom layer (Fig. 5).

#### IV. ELECTRONIC STRUCTURE

##### A. Twist-angles close to $0^\circ$

The electronic band structure plotted in the moiré Brillouine zone (MBZ) is a result of folding of bands from the UBZ of the individual layers (Fig. 1 (c) and (d)). It is hence

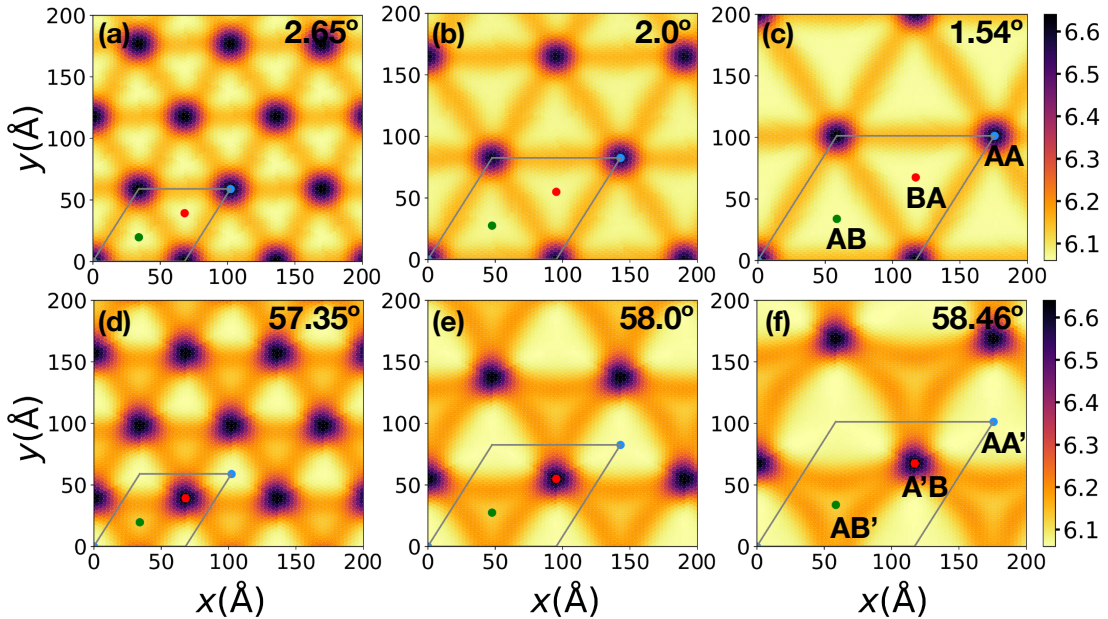


FIG. 4. (a), (b) and (c) ((d), (e) and (f)) Interlayer spacing distribution in  $2.65^\circ$ ,  $2.0^\circ$  and  $1.54^\circ$  ( $57.35^\circ$ ,  $58.0^\circ$  and  $58.46^\circ$ ) twisted bilayer MoS<sub>2</sub>, respectively.

essential to distinguish pure band-folding effects from that of flattening of the bands due to the moiré. We thus separately compute the band structure of pure AA' stacking in the same superlattice. Fig. 6 (a) shows bands of pure AA' stacking folded into the MBZ and also the band structure of the  $2.65^\circ$  TBM. The bands of TBM are clearly flatter than those of pure AA' stacking of same supercell size. The bands flatten due to the localisation of the corresponding electronic states in real-space. The valence band edge states, v1 and v2 in inset of Fig. 6 (a) are degenerate at the  $K$  point of the MBZ corresponding to the symmetry of the underlying lattice. This degeneracy at the  $K$  point is present in all twist angles close to  $0^\circ$  in our study (Fig. 7). The dispersion of the v1 and v2 valence bands is similar to graphene due to the localisation of these states in a hexagonal pattern, avoiding the AA stacking region, as shown in Fig. 6. Similar to graphene, the degeneracy at the  $K$  point is broken by the application of an external uniaxial strain to the moiré.

The localization of the bands at the valence band edge occurs due to inhomogeneous hybridization between the two layers in the moiré. As discussed previously<sup>19</sup>, this can be qualitatively understood in terms of ordering of the VBM with respect to the vacuum level

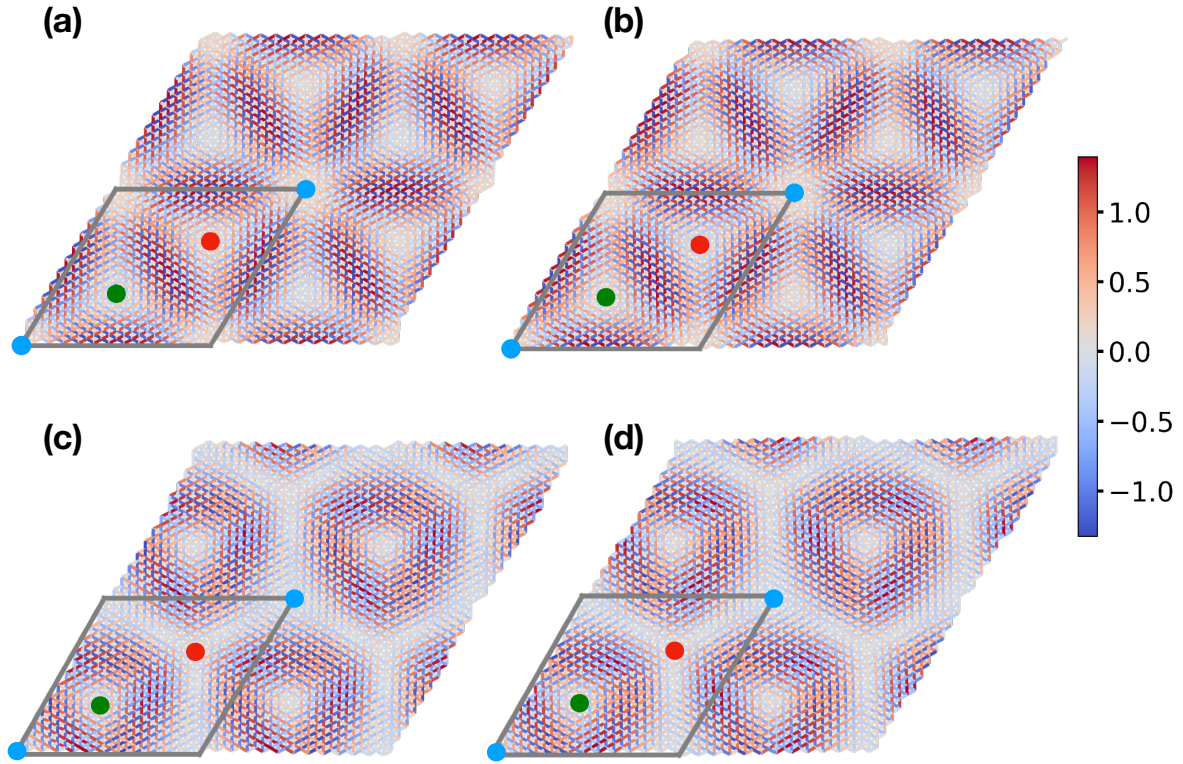


FIG. 5. (a) and (b) ((c) and (d)) Distribution of strains in the bottom and top layer of  $2.65^\circ$  ( $57.35^\circ$ ) TBM. A line is drawn connecting each Mo to its six nearest neighbors. The color of the line shows the strain in that direction. The dots in correspond to the location of high-symmetry stackings in the twisted bilayer.

amongst different high-symmetry stackings (see Fig. 2). The ordering of the VBM among the stackings is determined by splittings at the  $\Gamma$  point in the UBZ (Fig. 2). Since the AA and A'B stackings have lower VBM (with respect to vacuum) compared to the other stackings, they cannot contribute to the VBM of the moiré superlattice. The conduction band edge lines up among the stackings and provides no hint at a preferred localisation site. We can use the DFT potential barrier between the layers of a stacking as a measure of the interlayer hybridization for that stacking (Fig. 2). The extent of hybridization between the layers is inversely proportional to the DFT potential barrier between the layers. To create a map of the local potential barrier between the layers of the moiré, we construct a Voronoi diagram using the Mo atoms of the bottom layer. The self-consistent DFT potential,  $V(x, y, z)$ , of

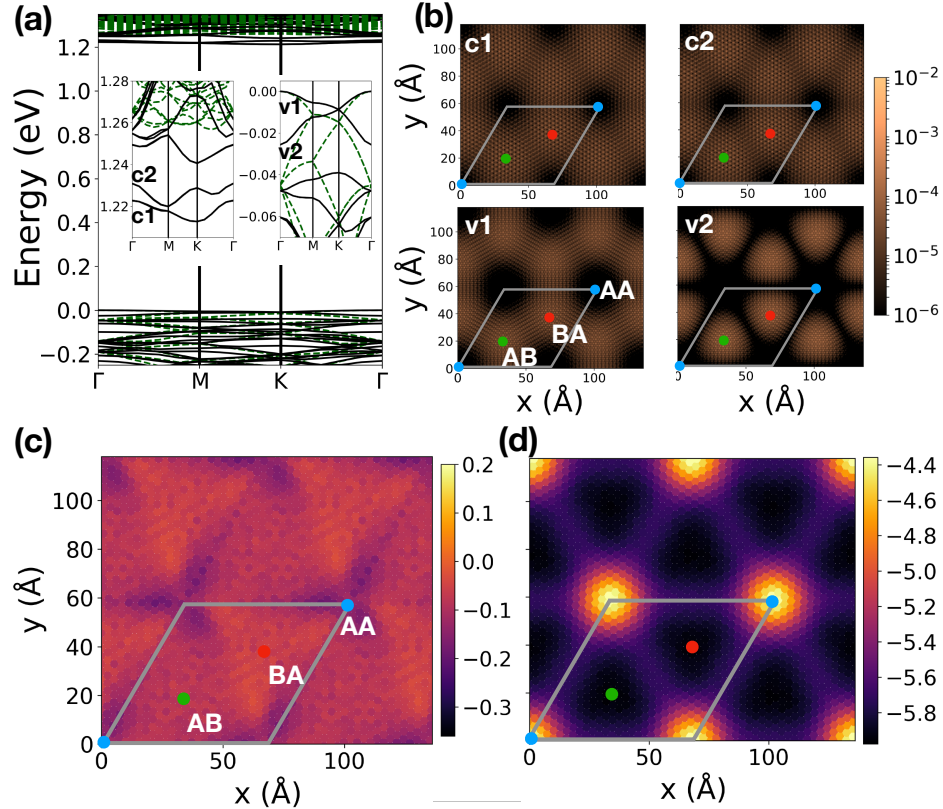


FIG. 6. Electronic structure of  $2.65^\circ$  TBM. (a) Band structure (black) of  $2.65^\circ$  TBM. Green dashed lines show band structure of purely AA' stacked bilayer MoS<sub>2</sub> in the same superlattice. The insets show plots of the valence and conduction band edges. (f) Charge density,  $|\psi_\Gamma|^2$ , of the states labeled in the inset of (a). The charge density is averaged in the out-of-plane direction. (c)  $\Delta V(x_{\text{Mo}}, y_{\text{Mo}})$  (in eV), for  $2.65^\circ$  TBM. (d) Distribution of the local potential barrier (in eV) between the layers,  $V_{\text{barr}}(x_{\text{Mo}}, y_{\text{Mo}})$ , in the moiré. The extent of hybridization between the layers is inversely proportional to the barrier.

the moiré is then planar averaged in each Voronoi cell individually to obtain  $V(x_{\text{Mo}}, y_{\text{Mo}}, z)$ .  $(x_{\text{Mo}}, y_{\text{Mo}})$  are the coordinates of the Mo atoms in the bottom layer. The barrier potential is then obtained for each Voronoi cell giving  $V_{\text{barr}}(x_{\text{Mo}}, y_{\text{Mo}})$ . The distribution of  $V_{\text{barr}}(x_{\text{Mo}}, y_{\text{Mo}})$  in Fig. 6 (d) shows the inhomogeneous hybridisation between the layers. As expected, the barrier is lowest for AB and BA, and highest for the AA stacking region. Neglecting structural relaxations leads to a spurious energy-separated flatband at the valence band edge (Fig. 8). This flatband is localised at the high-energy stacking regions, AA or A'B, for twist angle close to  $0^\circ$  or  $60^\circ$ , respectively (Fig. 8). The origin of this localisation is

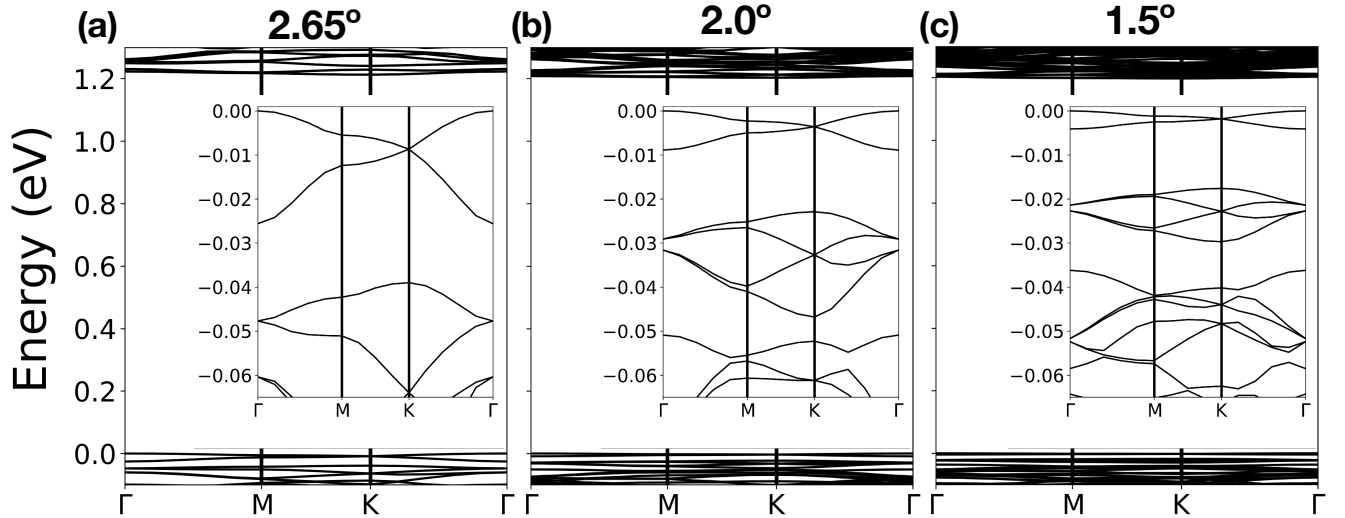


FIG. 7. (a), (b) and (c) Band structure of  $2.65^\circ$ ,  $2.0^\circ$  and  $1.5^\circ$  TBM. The insets show enlarged plot of the bands close to the valence band edge.

also inhomogeneous hybridisation in the rigidly-twisted moiré pattern. Due to the absence of varying interlayer spacing in the moiré, the ordering of the VBM among the unit-cell stackings is reversed<sup>19</sup>. This leads to localisation at the AA stacking.

### B. Twist-angles close to $60^\circ$

In  $58^\circ$  relaxed TBM, several ultraflatbands form at the valence and conduction band edges (Fig. 9 (a)) and are well separated in energy. The states close to the valence band edge localise at the AA' stacking and conduction band edge states at AB' (Fig. 9 (b) and (c)). The spatial distribution of the wavefunctions can be understood in terms of an infinite equilateral triangle well potential. A quantum particle in such a well (of side  $a$ ) can be described using two quantum numbers,  $p$  and  $q$ . The energies are given by  $E_{p,q} = (p^2 + q^2 + pq)E_0$ <sup>57</sup>,  $q$  takes the values  $0, 1/3, 2/3, 1, \dots$  and  $p = q + 1, q + 2, q + 3, \dots$ . The ground state,  $E_{1,0} = E_0 = 2\hbar^2/3ma^2$ . The eigenfunctions can be further labelled by  $A_1$ ,  $A_2$  and  $E$ . The  $A_1$  and  $A_2$  states are singly degenerate, while the  $E$  states are doubly degenerate<sup>57,58</sup>. In  $58^\circ$  TBM, the wavefunctions and degeneracies of the first six states (v1-v6) close to the valence band edge are in excellent agreement with those of the ground state and first five excited states of the infinite triangle potential well (Fig. 9 (b)). Similarly the

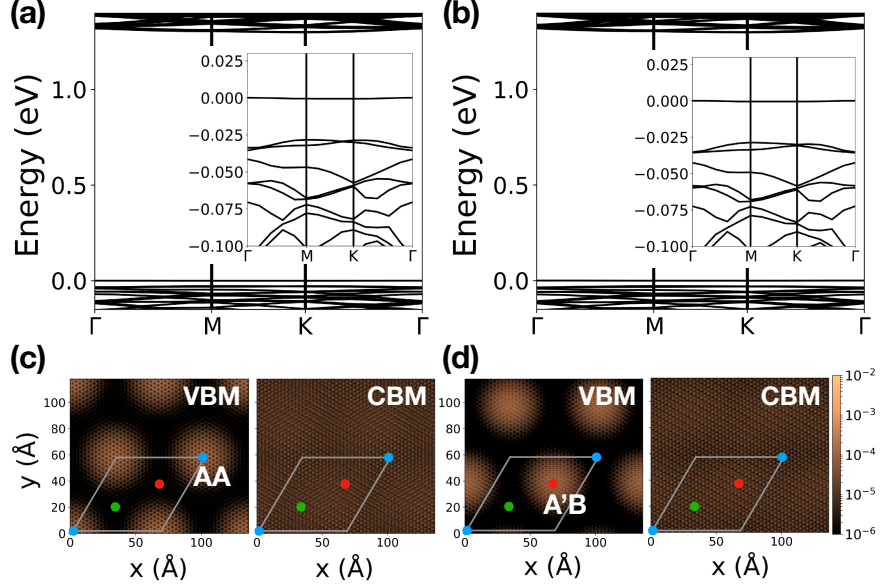


FIG. 8. Spurious localisation in rigidly-twisted structures. (a) and (b) Band structure of  $2.65^\circ$  and  $57.35^\circ$  rigidly (unrelaxed) twisted bilayer MoS<sub>2</sub>, respectively. The interlayer spacing is fixed at  $6.3\text{ \AA}$ . The inset shows an enlarged plot of the valence band edge. (c) and (d) Distribution of valence band maximum and conduction band minimum wavefunctions,  $|\psi|^2$ , of band structures shown in (a) and (b), respectively.

conduction band edge states also agree well, however the degeneracies do not follow those of the infinite triangle well. c1 and c2 both are doubly degenerate and correspond to  $\psi_{1,0}^{A_1}$  of the triangular well. These states have a valley degeneracy associated with them. The four states that make up c1 and c2 are folded in from the  $K$  and  $K'$  points of the UBZ of the top and bottom layer. The  $K$  point wavefunction in the monolayer is strongly localised in the out-of-plane direction<sup>47</sup>. Weak interlayer hybridization leads to a small gap opening between the c1 and c2 states. c3 is four-fold degenerate, and has an envelope function with a node at the center of the well (Fig. 9 (c)) resembling  $\psi_{\frac{4}{3},\frac{1}{3}}^E$ . The six degenerate states are a result of the folding of the  $\Lambda$  point (between  $\Gamma$  and  $K$ ) valley in the UBZ. The states close to the valence band edge fold only from the  $\Gamma$  point of the UBZ. The degeneracies are hence unaffected and follow those of the infinite triangular well. It should be noted that in contrast to the ideal infinite triangle potential well, the potential in moiré is periodic and of finite depth. We thus expect only a few states close to the valence and conduction band edge to be confined in a triangular region.

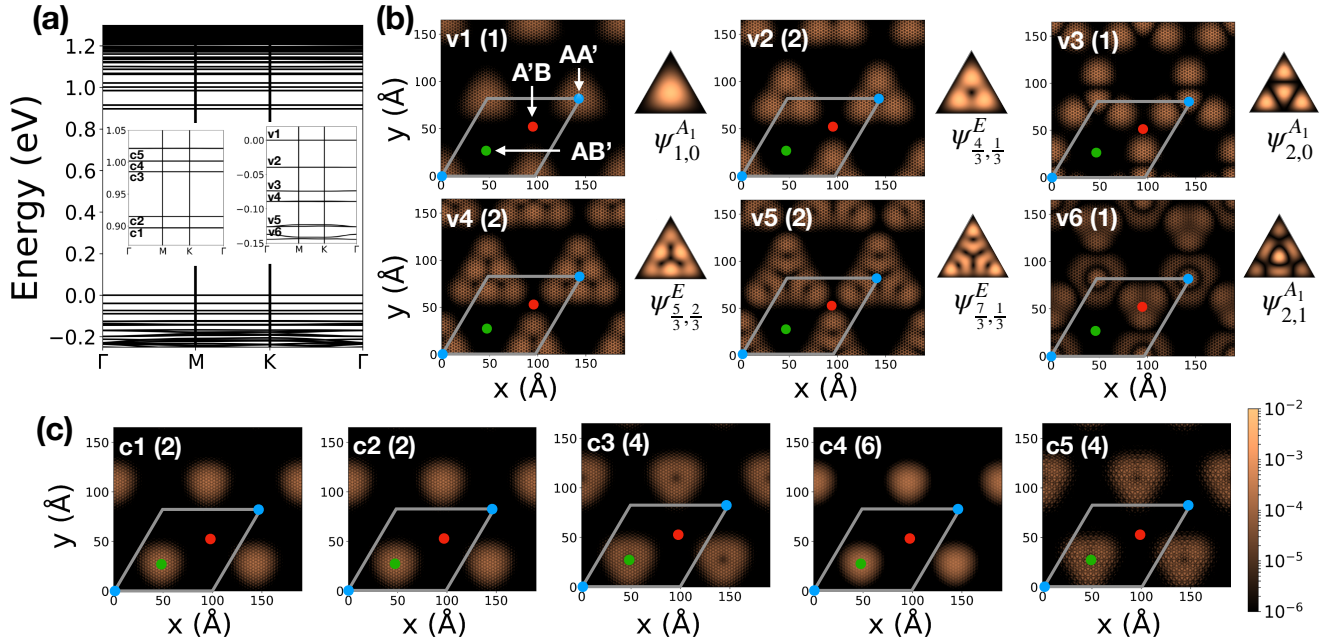


FIG. 9. Electronic structure of 58° TBM. (a) Band structure of 58° TBM showing the multiple energy-separated ultraflatbands. The inset shows and labels the flatbands close to the valence and conduction band edges. (b) Distribution,  $|\psi_\Gamma(\mathbf{r})^2|$ , of the states labeled in (a), averaged in the out-of-plane ( $z$ ) direction. The corresponding equilateral triangle quantum well wavefunctions of the ground state ( $\psi_{1,0}^{A_1}$ ) and first five excited states are shown alongside. (c)  $|\psi_\Gamma(\mathbf{r})^2|$  of the conduction states labeled in (a), c1-c5, averaged along the  $z$ -direction. The degeneracies of the wavefunctions in (b) and (e) are shown in brackets.

We also study the effect of the structural reconstruction on the electronic structure of the individual layers. Fig. 10 shows the electronic structure of the puckered bottom layer of relaxed 57.35° moiré. The strains (Fig. 5) in the layer leads to localisation of the band edge states (Fig. 10). As opposed to the bilayer, the valence and conduction bands in the monolayer fold in from the optically active  $K$  point in the UBZ. The localisation of the  $K$  point wavefunctions strongly suggests the modification of excitonic properties of these systems. This could explain the recent discovery of moiré excitons in twisted bilayer TMDs<sup>24,42-46</sup>.

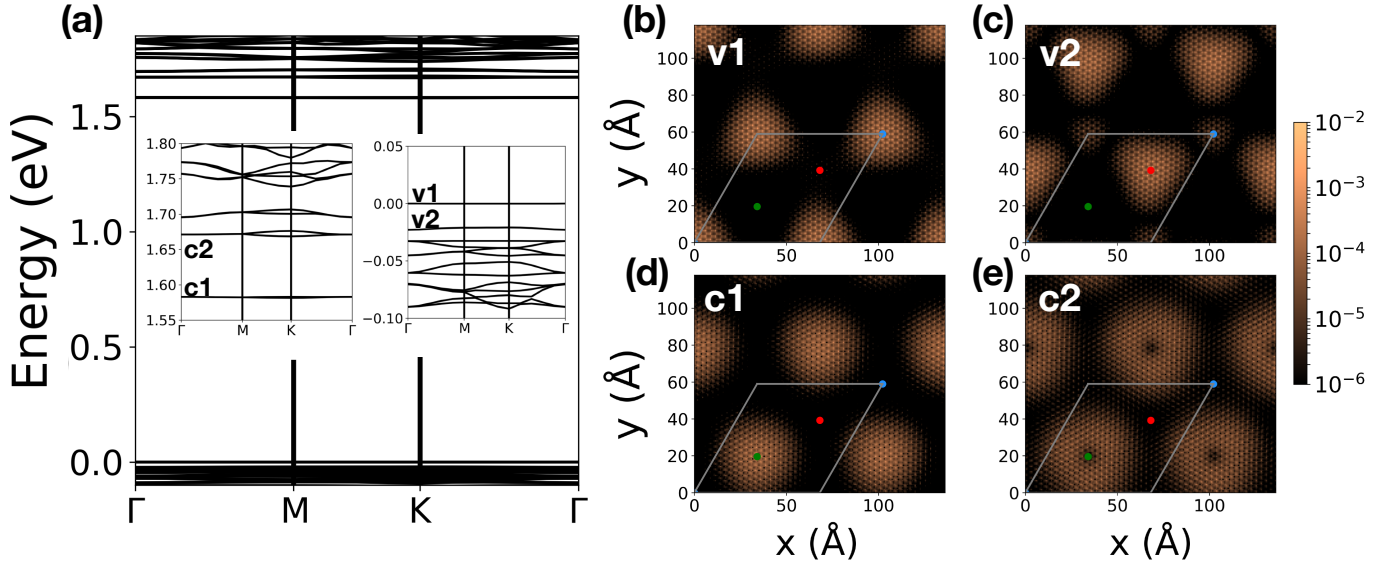


FIG. 10. Electronic structure modification of individual layers. (a) Bandstructure of the bottom layer of relaxed  $57.35^\circ$  moiré superlattice. The inset shows the bands close to the valence and conduction band edge. The band edge states are folded in from the  $K$  point of the unit-cell BZ. (b) Distribution of valence band edge ( $v_1$  and  $v_2$ ) and conduction band edge ( $c_1$  and  $c_2$ ) wavefunctions corresponding to the states shown in (a).

### C. Origin of triangular quantum dots

To understand the origin of the triangular quantum well potential, we plot the distribution of  $V_{\text{barr}}(x_{\text{Mo}}, y_{\text{Mo}})$  (Fig. 11 (c) and (d)), which shows the inhomogeneous hybridisation between the layers. As expected, the barrier is lowest for AA', AB' regions and highest for the A'B stacking region (Fig. 2). This suggests localisation of the valence band edge states at the AA' and AB' regions in the moiré. However, the valence band edge states localise at the AA' stacking alone and conduction band edge states at AB' (Fig. 9 (b) and (c)). We find that in addition to the inhomogeneous hybridization, a modulating potential is introduced in the moiré for twist angles close to  $60^\circ$  which explains the localisation pattern. To calculate the modulating potential, we first average the DFT potential in a slab of length 17 Å in the out-of-plane direction containing the bilayer, to obtain  $V_M(x, y)$ . We then macroscopic average  $V_M(x, y)$ , as discussed above, to obtain  $V_M(x_{\text{Mo}}, y_{\text{Mo}})$ . The confining potential with respect to AA' stacking is given by:  $\Delta V(x_{\text{Mo}}, y_{\text{Mo}}) = V_M(x_{\text{Mo}}, y_{\text{Mo}}) - \bar{V}_{\text{AA}'}$ . Where  $\bar{V}_{\text{AA}'}$  is unit-cell averaged potential of AA' stacking.  $\Delta V(x_{\text{Mo}}, y_{\text{Mo}})$  has a minimum

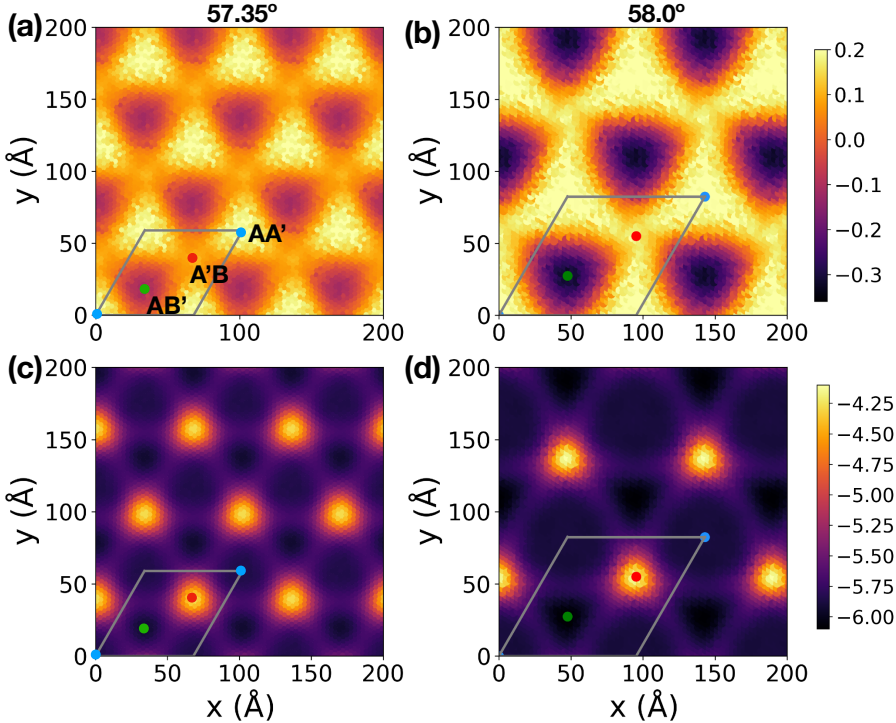


FIG. 11. (a) and (b) Confining potential,  $\Delta V(x_{\text{Mo}}, y_{\text{Mo}})$ , for  $57.35^\circ$  and  $58^\circ$  TBM, respectively. (c) and (d) Local potential barrier distribution (in eV) between the layers,  $V_{\text{barr}}(x_{\text{Mo}}, y_{\text{Mo}})$ , in  $57.35^\circ$  and  $58^\circ$  TBM.

at the  $\text{AB}'$  site, which confines the electrons (Fig. 9 (c)), and a maximum at  $\text{A}'\text{B}$  and  $\text{AA}'$ . The inhomogeneous hybridization rules out localisation at  $\text{A}'\text{B}$ , hence inducing the holes to localise at the  $\text{AA}'$  stacking. The confining potential has the shape of an equilateral triangle (Fig. 11 (a) and (b)). No modulation in  $\Delta V(x_{\text{Mo}}, y_{\text{Mo}})$  is found for twist angles close to  $0^\circ$ . These structures correspondingly have no localisation at the conduction band edge. Hence the electronic structure for twist angles close to  $0^\circ$  is very different from that close to  $60^\circ$ .

To understand the origin of the confining triangular potential in twist angles close to  $60^\circ$  we probe the role of local strains in the moiré. The strain is localised at the shear soliton regions in each layer (Fig. 5). We can construct a strain-free moiré by allowing atomic relaxations only in the out-of-plane direction (from the rigidly twisted moiré superlattice). The interlayer spacing is allowed to vary in this procedure (Fig. 12 (b)), hence the ordering of the VBM among the stackings is preserved. We find that in this structure the multiple energy-separated ultraflatbands in  $57.35^\circ$  vanish (Fig. 12 (c) and (d)). The conduction bands are delocalised due to the absence of a modulating potential well and the valence bands

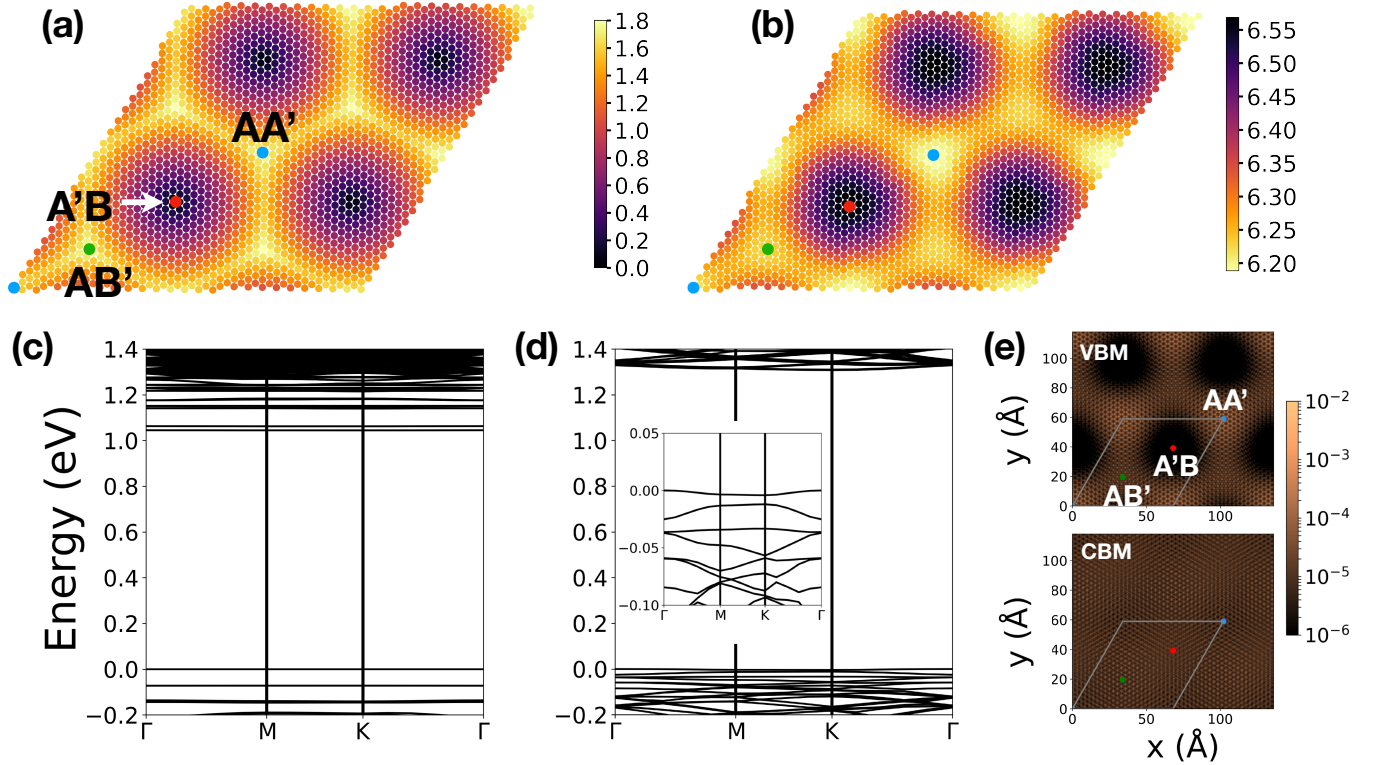


FIG. 12. Effect of constrained relaxation in  $57.35^\circ$  TBM. (a) and (b) Distribution of order-parameter and interlayer spacing in  $57.35^\circ$  TBM with constrained relaxation (only out-of-plane relaxations are allowed), respectively. (c) and (d) Band structure of  $57.35^\circ$  TBM with full relaxation and constrained relaxation, respectively. (e)  $|\psi|^2$  distribution of VBM and CBM wavefunctions, averaged along the out-of-plane direction, for the band structure in (d).

are localised at the AA' and AB' sites (Fig. 12 (e)), as expected from the hybridization arguments.  $V_{\text{barr}}(x_{\text{Mo}}, y_{\text{Mo}})$  and  $\Delta V(x_{\text{Mo}}, y_{\text{Mo}})$  for this structure are shown in Fig. 13. This clearly establishes in-plane relaxations, leading to strains, as the driving mechanism for formation of the modulating potential well, which in turn determines localisation of the wavefunctions. The localisation in  $2.65^\circ$  TBM, on the other hand, is not affected by constrained relaxation (Fig. 14).

#### D. Evolution of electronic structure with twist angle

Fig. 15 shows evolution of the flatbands for twist angles  $57.35^\circ$ ,  $58.0^\circ$  and  $58.5^\circ$ . As the twist angle approaches  $60^\circ$ , the AA' stacking area grows larger than the other stackings

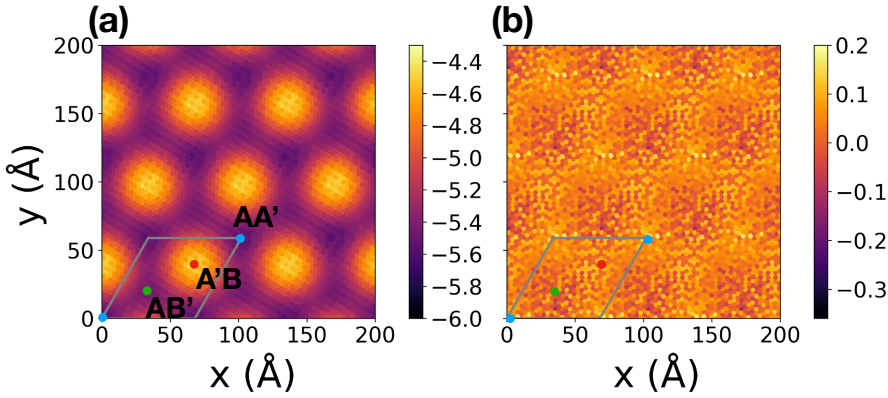


FIG. 13. (a) and (b) Distribution of  $V_{\text{barr}}(x_{\text{Mo}}, y_{\text{Mo}})$  and  $\Delta V(x_{\text{Mo}}, y_{\text{Mo}})$  in constrain relaxed (only out-of-plane relaxations are allowed)  $57.35^\circ$  TBM, respectively.

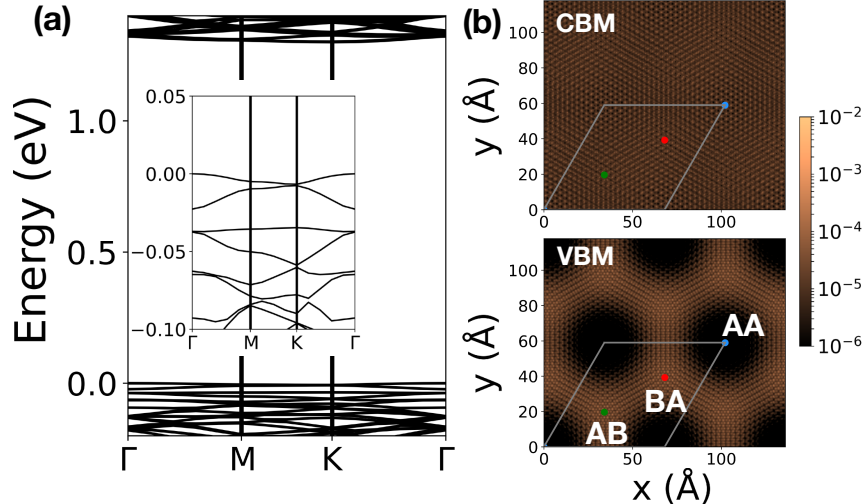


FIG. 14. Effect of constrained relaxation in  $2.65^\circ$  TBM. (a) Band structure of  $2.65^\circ$  TBM with constrained relaxation of the superlattice (only out-of-plane relaxations). (b)  $|\psi|^2$  distribution of VBM and CBM wavefunctions, averaged along the out-of-plane direction, for the band structure in (a).

(Fig. 3). As the area of confinement of holes increases, the spacing between the flatbands close to valence band edge decreases as shown in Fig. 15 (b). While the area of  $\text{AB}'$  region does not grow appreciably as the twist angle approaches  $60^\circ$  (Fig. 3), the confining potential depth increases (Fig. 11). The spacings between levels at the conduction band edge are thus relatively unaffected (Fig. 15 (b)). Furthermore, the band gap of the moiré superlattice reduces as the twist angle approaches  $60^\circ$ . While the band gap shown in Fig. 15

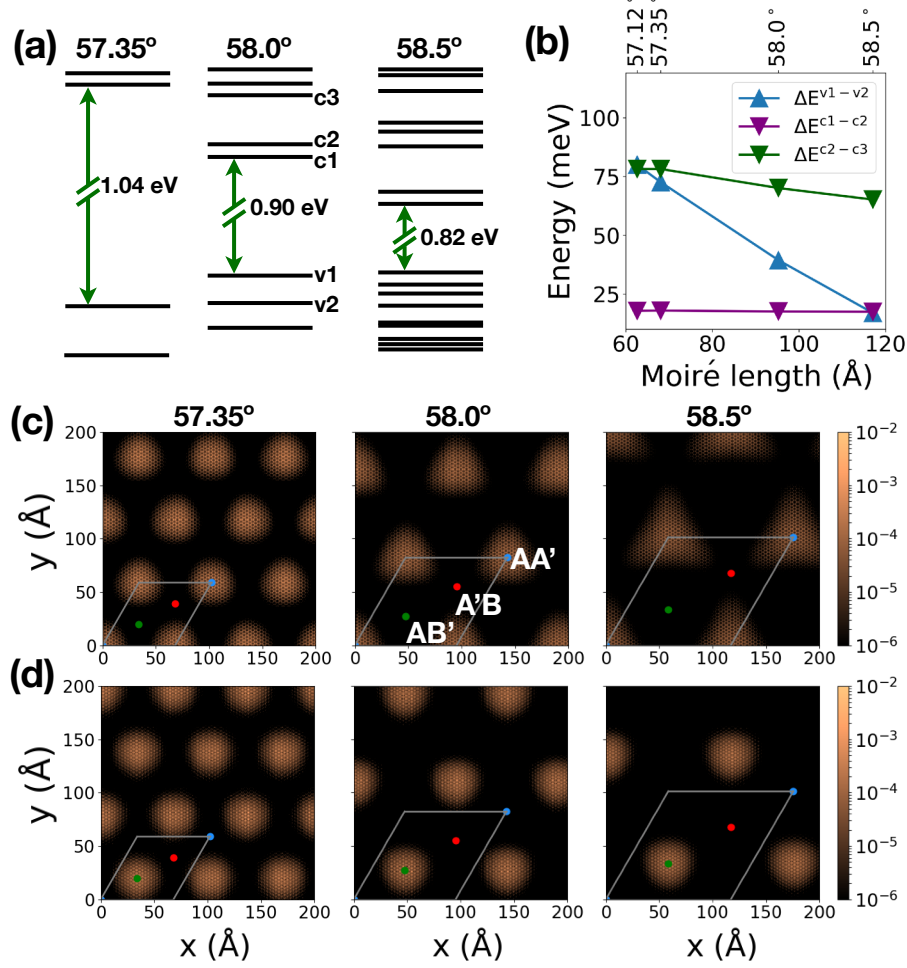


FIG. 15. Evolution of electronic structure with twist angle. (a) Evolution of ultraflatbands close to the valence and conduction band edge for twist angles  $57.35^\circ$ ,  $58.0^\circ$  and  $58.5^\circ$ . The band gap is not to scale and is shown using a green arrow. (b) Evolution of the splittings between the first two states at the valence band edge,  $\Delta E^{v1-v2}$ , first ( $\Delta E^{c1-c2}$ ) and second two states ( $\Delta E^{c2-c3}$ ) at the conduction band edge. (c) ((d)) The wavefunction distribution of the v1 (c1) state in the moiré, averaged along the out-of-plane direction, for the three twist angles.

(a) is the bandgap of the entire moiré, the band gap also varies locally in the moiré pattern. The valence and conduction band edge energy for each local stacking is different due to the presence of the confining potential well. The valence band edge energy is highest at the AB stacking region and the conduction band edge is lowest at the AB' stacking. This spatial variation in the local density of states has been captured by scanning tunneling spectroscopy measurements of moiré superlattices<sup>59,60</sup>.

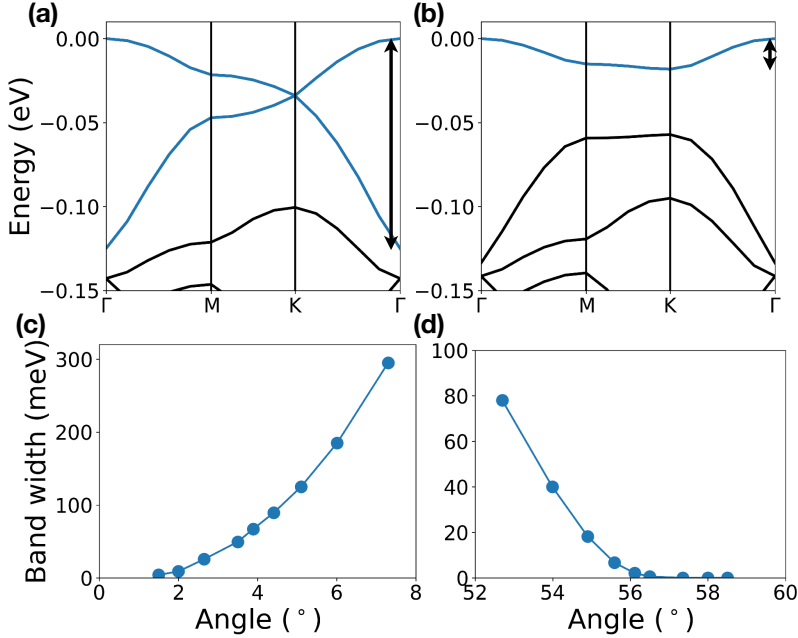


FIG. 16. (a) and (b) Bandstructure of  $5.1^\circ$  and  $54.9^\circ$  TBM, close to the valence band edge, respectively. The bandwidth is measured for the first two bands in (a) and the first band in (b). (c) and (d) Band width (defined as shown in (a) and (b)) as a function of twist angle between MoS<sub>2</sub> layers.

The wavefunction localisation of the band edge states for  $57.35^\circ$ ,  $58.0^\circ$  and  $58.5^\circ$  twist angles is shown in Fig. 15 (c) and (d). The evolution of these states from  $7.3^\circ$  to  $1.5^\circ$  and  $52.7^\circ$  to  $58.5^\circ$  have been compiled into a movie available<sup>61</sup> in the supplementary materials. The states at the band edges can be regarded as triangular quantum dot states for twist-angles greater than  $56^\circ$ . The real-space confinement of the wavefunctions leads to reduction in the band width of these states. The band width of the first flatband at the valence band edge reduces monotonically as the twist angle approaches  $0^\circ$  or  $60^\circ$  as shown in Fig. 16. The flatbands for twist angles greater than  $56^\circ$  are nearly dispersionless with bandwidth less than 1 meV. This evolution clearly indicates the absence of unique "magic" angles for flatband formation in TBM.

We also study the evolution of the first four flat bands at the valence band edge for twist angles close to  $0^\circ$  (Fig. 17). The wavefunctions for twist angles close to  $0^\circ$  always avoid the AA stacking region, as expected from the inhomogeneous hybridisation in the moiré. The localisation patterns could be considered as solutions to a more complex periodic potential

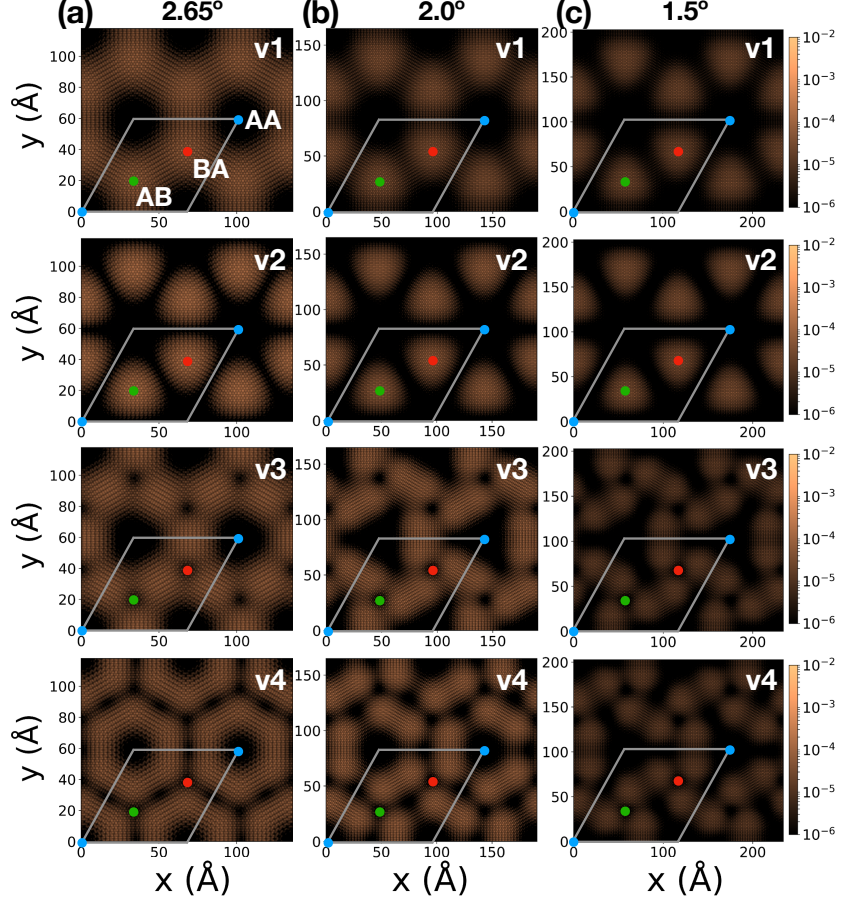


FIG. 17. (a), (b) and (c) Distribution of the valence band wavefunctions of TBM, averaged in the out-of-plane direction, for twist angles  $2.65^\circ$ ,  $2.0^\circ$  and  $1.5^\circ$ , respectively. The  $|\psi|^2$  distribution of the first four valence states are plotted at the  $\Gamma$  point.

well with minima at the AB and BA sites. The flatbands close to the valence and conduction band edge for twist angle close to  $60^\circ$ , on the other hand, behave like triangular quantum dots as discussed above.

## V. CONCLUSION

We have demonstrated the formation of an array of triangular quantum dots in moiré patterns of TBM for twist angles close to  $60^\circ$ . The holes and electrons are spatially separated which could lead to long-lifetime confined excitons in this system. By probing the origin and evolution of the ultraflatbands we conclude that no special magic angles exist in TBM like they do in twisted bilayer graphene. This makes it easier to experimentally probe

ultraflatbands in these systems. The contrasting electronic structure of twist angles close to  $0^\circ$  and  $60^\circ$  is due to an additional modulating confining potential in twist angles close to  $60^\circ$ . In-plane structural reconstruction of the moiré is responsible for the formation of this confining potential. External strains can thus be used to engineer the confining potential and flatbands in these systems.

## ACKNOWLEDGMENTS

The authors thank the Supercomputer Education and Research Centre (SERC) at IISc for providing the computational facilities.

---

\* Present address: Department of Physics, University of California at Berkeley, California 94720, USA and Materials Sciences Division, Lawrence Berkeley National Laboratory, Berkeley, California 94720, USA.

† mjain@iisc.ac.in

- <sup>1</sup> Y. Cao, V. Fatemi, S. Fang, K. Watanabe, T. Taniguchi, E. Kaxiras, and P. Jarillo-Herrero, Nature (2018).
- <sup>2</sup> Y. Cao, V. Fatemi, A. Demir, S. Fang, S. L. Tomarken, J. Y. Luo, J. D. Sanchez-Yamagishi, K. Watanabe, T. Taniguchi, E. Kaxiras, R. C. Ashoori, and P. Jarillo-Herrero, Nature (2018).
- <sup>3</sup> R. Bistritzer and A. H. MacDonald, Proceedings of the National Academy of Sciences **108**, 12233 (2011).
- <sup>4</sup> H. C. Po, L. Zou, A. Vishwanath, and T. Senthil, Phys. Rev. X **8**, 031089 (2018).
- <sup>5</sup> G. Tarnopolsky, A. J. Kruchkov, and A. Vishwanath, Phys. Rev. Lett. **122**, 106405 (2019).
- <sup>6</sup> Y. W. Choi and H. J. Choi, Phys. Rev. B **98**, 241412 (2018).
- <sup>7</sup> Y. Su and S.-Z. Lin, Phys. Rev. B **98**, 195101 (2018).
- <sup>8</sup> J. González and T. Stauber, Phys. Rev. Lett. **122**, 026801 (2019).
- <sup>9</sup> C. Xu and L. Balents, Phys. Rev. Lett. **121**, 087001 (2018).
- <sup>10</sup> F. Wu, A. H. MacDonald, and I. Martin, Phys. Rev. Lett. **121**, 257001 (2018).
- <sup>11</sup> D. M. Kennes, J. Lischner, and C. Karrasch, Phys. Rev. B **98**, 241407 (2018).
- <sup>12</sup> F. Conte, D. Ninno, and G. Cantele, Phys. Rev. B **99**, 155429 (2019).

- <sup>13</sup> N. R. Chebrolu, B. L. Chittari, and J. Jung, Phys. Rev. B **99**, 235417 (2019).
- <sup>14</sup> F. Haddadi, Q. Wu, A. J. Kruchkov, and O. V. Yazyev, arXiv e-prints , arXiv:1906.00623 (2019), arXiv:1906.00623 [cond-mat.mes-hall].
- <sup>15</sup> L. Xian, D. M. Kennes, N. Tancogne-Dejean, M. Altarelli, and A. Rubio, Nano Letters **0**, null (0).
- <sup>16</sup> P. Kang, W.-T. Zhang, V. Michaud-Rioux, X.-H. Kong, C. Hu, G.-H. Yu, and H. Guo, Phys. Rev. B **96**, 195406 (2017).
- <sup>17</sup> D. M. Kennes, L. Xian, M. Claassen, and A. Rubio, arXiv e-prints , arXiv:1905.04025 (2019), 1905.04025.
- <sup>18</sup> X.-J. Zhao, Y. Yang, D.-B. Zhang, and S.-H. Wei, arXiv e-prints , arXiv:1906.05992 (2019), arXiv:1906.05992.
- <sup>19</sup> M. H. Naik and M. Jain, Phys. Rev. Lett. **121**, 266401 (2018).
- <sup>20</sup> F. Wu, T. Lovorn, E. Tutuc, and A. H. MacDonald, Phys. Rev. Lett. **121**, 026402 (2018).
- <sup>21</sup> S. Carr, S. Fang, Z. Zhu, and E. Kaxiras, Phys. Rev. Research **1**, 013001 (2019).
- <sup>22</sup> Z. A. H. Goodwin, F. Corsetti, A. A. Mostofi, and J. Lischner, arXiv e-prints , arXiv:1905.01887 (2019), arXiv:1905.01887.
- <sup>23</sup> K. Tran, G. Moody, F. Wu, X. Lu, J. Choi, K. Kim, A. Rai, D. A. Sanchez, J. Quan, A. Singh, J. Embley, A. Zepeda, M. Campbell, T. Autry, T. Taniguchi, K. Watanabe, N. Lu, S. K. Banerjee, K. L. Silverman, S. Kim, E. Tutuc, L. Yang, A. H. MacDonald, and X. Li, Nature **567**, 71 (2019).
- <sup>24</sup> E. M. Alexeev, D. A. Ruiz-Tijerina, M. Danovich, M. J. Hamer, D. J. Terry, P. K. Nayak, S. Ahn, S. Pak, J. Lee, J. I. Sohn, M. R. Molas, M. Koperski, K. Watanabe, T. Taniguchi, K. S. Novoselov, R. V. Gorbachev, H. S. Shin, V. I. Fal'ko, and A. I. Tartakovskii, Nature **567**, 81 (2019).
- <sup>25</sup> F. Gargiulo and O. V. Yazyev, 2D Materials **5**, 015019 (2018).
- <sup>26</sup> M. H. Naik, I. Maity, P. K. Maiti, and M. Jain, The Journal of Physical Chemistry C **123**, 9770 (2019).
- <sup>27</sup> I. Maity, M. H. Naik, P. K. Maiti, H. R. Krishnamurthy, and M. Jain, Phys. Rev. Research **2**, 013335 (2020).
- <sup>28</sup> S. Carr, D. Massatt, S. B. Torrisi, P. Cazeaux, M. Luskin, and E. Kaxiras, Phys. Rev. B **98**, 224102 (2018).

- <sup>29</sup> A. Weston, Y. Zou, V. Enaldiev, A. Summerfield, N. Clark, V. Zólyomi, A. Graham, C. Yelgel, S. Magorrian, M. Zhou, J. Zultak, D. Hopkinson, A. Barinov, T. H. Bointon, A. Kretinin, N. R. Wilson, P. H. Beton, V. I. Fal'ko, S. J. Haigh, and R. Gorbachev, *Nature Nanotechnology* (2020).
- <sup>30</sup> M. R. Rosenberger, H.-J. Chuang, M. Phillips, V. P. Oleshko, K. M. McCreary, S. V. Sivaram, C. S. Hellberg, and B. T. Jonker, *ACS Nano* **14**, 4550 (2020), pMID: 32167748.
- <sup>31</sup> R. C. Ashoori, *Nature* **379**, 413 (1996).
- <sup>32</sup> U. Banin, Y. Cao, D. Katz, and O. Millo, *Nature* **400**, 542 (1999).
- <sup>33</sup> H. Yu, G.-B. Liu, J. Tang, X. Xu, and W. Yao, *Science Advances* **3** (2017), 10.1126/sci-adv.1701696.
- <sup>34</sup> S. Xu, D. Li, and P. Wu, *Advanced Functional Materials* **25**, 1127 (2015).
- <sup>35</sup> D. Gopalakrishnan, D. Damien, and M. M. Shaijumon, *ACS Nano* **8**, 5297 (2014).
- <sup>36</sup> Z. Gan, Q. Gui, Y. Shan, P. Pan, N. Zhang, and L. Zhang, *Journal of Applied Physics* **120**, 104503 (2016).
- <sup>37</sup> C. Perumal Veeramalai, F. Li, T. Guo, and T. W. Kim, *Dalton Trans.* **48**, 2422 (2019).
- <sup>38</sup> H. D. Ha, D. J. Han, J. S. Choi, M. Park, and T. S. Seo, *Small* **10**, 3858 (2014).
- <sup>39</sup> H. Lin, C. Wang, J. Wu, Z. Xu, Y. Huang, and C. Zhang, *New J. Chem.* **39**, 8492 (2015).
- <sup>40</sup> M. Wu, X. Qian, and J. Li, *Nano Letters* **14**, 5350 (2014).
- <sup>41</sup> M. Fleischmann, R. Gupta, S. Sharma, and S. Shallcross, arXiv e-prints , arXiv:1901.04679 (2019), 1901.04679.
- <sup>42</sup> K. L. Seyler, P. Rivera, H. Yu, N. P. Wilson, E. L. Ray, D. G. Mandrus, J. Yan, W. Yao, and X. Xu, *Nature* **567**, 66 (2019).
- <sup>43</sup> C. Jin, E. C. Regan, A. Yan, M. Iqbal Bakti Utama, D. Wang, S. Zhao, Y. Qin, S. Yang, Z. Zheng, S. Shi, K. Watanabe, T. Taniguchi, S. Tongay, A. Zettl, and F. Wang, *Nature* **567**, 76 (2019).
- <sup>44</sup> K. Tran, G. Moody, F. Wu, X. Lu, J. Choi, K. Kim, A. Rai, D. A. Sanchez, J. Quan, A. Singh, J. Embley, A. Zepeda, M. Campbell, T. Autry, T. Taniguchi, K. Watanabe, N. Lu, S. K. Banerjee, K. L. Silverman, S. Kim, E. Tutuc, L. Yang, A. H. MacDonald, and X. Li, *Nature* **567**, 71 (2019).
- <sup>45</sup> E. C. Regan, D. Wang, C. Jin, M. I. B. Utama, B. Gao, X. Wei, S. Zhao, W. Zhao, K. Yumigeta, M. Blei, J. Carlstroem, K. Watanabe, T. Taniguchi, S. Tongay, M. Crommie, A. Zettl, and

- F. Wang, “Optical detection of mott and generalized wigner crystal states in wse2/ws2 moir superlattices,” (2019), arXiv:1910.09047 [cond-mat.mes-hall].
- <sup>46</sup> M. Brotons-Gisbert, H. Baek, A. Molina-Sánchez, D. Scerri, D. White, K. Watanabe, T. Taniguchi, C. Bonato, and B. D. Gerardot, arXiv e-prints , arXiv:1908.03778 (2019), 1908.03778.
- <sup>47</sup> M. H. Naik and M. Jain, Phys. Rev. B **95**, 165125 (2017).
- <sup>48</sup> <http://www.physics.iisc.ernet.in/~mjain/pages/software.html>.
- <sup>49</sup> <https://lammps.sandia.gov>.
- <sup>50</sup> S. Plimpton, Journal of Computational Physics **117**, 1 (1995).
- <sup>51</sup> F. H. Stillinger and T. A. Weber, Phys. Rev. B **31**, 5262 (1985).
- <sup>52</sup> J.-W. Jiang and Y.-P. Zhou, in *Handbook of Stillinger-Weber Potential Parameters for Two-Dimensional Atomic Crystals*, edited by J.-W. Jiang and Y.-P. Zhou (IntechOpen, Rijeka, 2017) Chap. 1.
- <sup>53</sup> W. Kohn and L. J. Sham, Phys. Rev. **140**, A1133 (1965).
- <sup>54</sup> J. M. Soler, E. Artacho, J. D. Gale, A. García, J. Junquera, P. Ordejón, and D. Sánchez-Portal, Journal of Physics: Condensed Matter **14**, 2745 (2002).
- <sup>55</sup> N. Troullier and J. L. Martins, Phys. Rev. B **43**, 1993 (1991).
- <sup>56</sup> M. M. van Wijk, A. Schuring, M. I. Katsnelson, and A. Fasolino, 2D Materials **2**, 034010 (2015).
- <sup>57</sup> W.-K. Li and S. M. Blinder, Journal of Chemical Education **64**, 130 (1987).
- <sup>58</sup> H. R. Krishnamurthy, H. S. Mani, and H. C. Verma, Journal of Physics A: Mathematical and General **15**, 2131 (1982).
- <sup>59</sup> C. Zhang, C.-P. Chuu, X. Ren, M.-Y. Li, L.-J. Li, C. Jin, M.-Y. Chou, and C.-K. Shih, Science Advances **3** (2017), 10.1126/sciadv.1601459.
- <sup>60</sup> C. Zhang, M.-Y. Li, J. Tersoff, Y. Han, Y. Su, L.-J. Li, D. A. Muller, and C.-K. Shih, Nature Nanotechnology **13**, 152 (2018).
- <sup>61</sup> See Supplementary Materials for movie showing the evolution of the flatband localisation with twist-angle.